

Hook-shaped structures to improve pool boiling heat transfer

Ahmed Elkholy^a, John Swift^b, Roger Kempers^{a,*}

^a Department of Mechanical Engineering, York University, Toronto, Canada

^b NUCAP Industries, Toronto, Canada

ARTICLE INFO

Keywords:

Two phase
Pool boiling
Heat transfer
Immersion cooling
Critical heat flux
Skiving
GRIPMetal

ABSTRACT

Boiling performance while using raised hook-shaped metal features, manufactured from copper by a skiving process, was investigated and compared with the boiling performance of a bare copper surface. Deionized water at the saturated conditions at 1 atm was used as the working medium. These fins can potentially improve the performance of immersion cooling spreaders in power electronics applications. The advantages of this technology compared with other methods presented in the literature include its scalability, low cost, resistance to erosion and clogging, and the industrialization of the manufacturing method. Four GRIPMetal hooked surfaces were investigated, each with different profiles (i.e., metal features, heights, and spacing) induced by the manufacturing process. The results show that the surface with hooks had lower wall superheat at the onset of nucleate boiling (ONB) compared with the bare surface. This appears to be due to the surface cavities—i.e., the negative portions of the raised hooks created by the skiving process, which helped initiate bubbles earlier. Moreover, the heat transfer coefficient (HTC) was superior for all surfaces with hooks at low heat fluxes because of increased surface area and enhanced bubble dynamics offered by the arrangement of the hooks. The hooked surface achieved a maximum HTC of 8.9 W/cm²K, which represents a 96 % enhancement ratio over the bare surface. The surface area increase (A_t/A_{bare}) offered by the proposed hooks and their corresponding grooves was measured using the photogrammetry technique and was found to range from 1.35 to 1.8. Lastly, the critical heat flux (CHF) was significantly enhanced, reaching a 67 % increase over the bare surface; this is attributed to the available bare inter-fin area that can supply the liquid to the nucleation sites and the assisted suction flow through the front of the grooves.

1. Introduction and background

Enhancing the rate of boiling heat transfer is crucial for many industrial applications such as HVAC, boilers, nuclear reactors, and electronics cooling. In the microelectronics industry, boiling-based cooling systems have recently garnered attention because of their ability to remove high heat flux, enabling the development of miniature components. Liquid immersion is an advanced boiling-based system in which the device being cooled is fully submerged in dielectric that works exactly the same as pool boiling. Such systems are characterized by their simplicity because of the absence of mechanical moving parts, resulting in operational cost reduction and reduced data center land use [1–3]. Two key metrics are used to characterize the performance of boiling surfaces: critical heat flux (CHF) and heat transfer coefficient (HTC). The main aim for any augmentation technique is to achieve a simultaneous improvement for both parameters. Many passive and active techniques have been investigated; in the last decade, many researchers have

studied passive techniques and surface modification because of these methods' simplicity, cost-effectiveness, and lack of reliance on external power sources.

Common surface modifications can be broadly categorized into four areas:

1. Increase of the heat transfer surface by adding fins [4,5] or grooves [6].
2. Addition of artificial nucleation sites by roughening the heater [7] or introducing dimples [8] and cavities [9].
3. Creation of capillaries or arteries to wick the liquid to the dry out spots, i.e., separate the vapor and liquid phases by creating a porous layer through sintering [10,11], deposition [12], or coating [13].
4. Engineering of the heater wettability by creating mixed patterns of hydrophilic/hydrophobic surface features (biphilic) [14,15].

Although some showed a drastic improvement, reaching 200–600 % of the HTC and CHF compared with bare surfaces [16–21], these

* Corresponding author.

E-mail address: kempers@yorku.ca (R. Kempers).

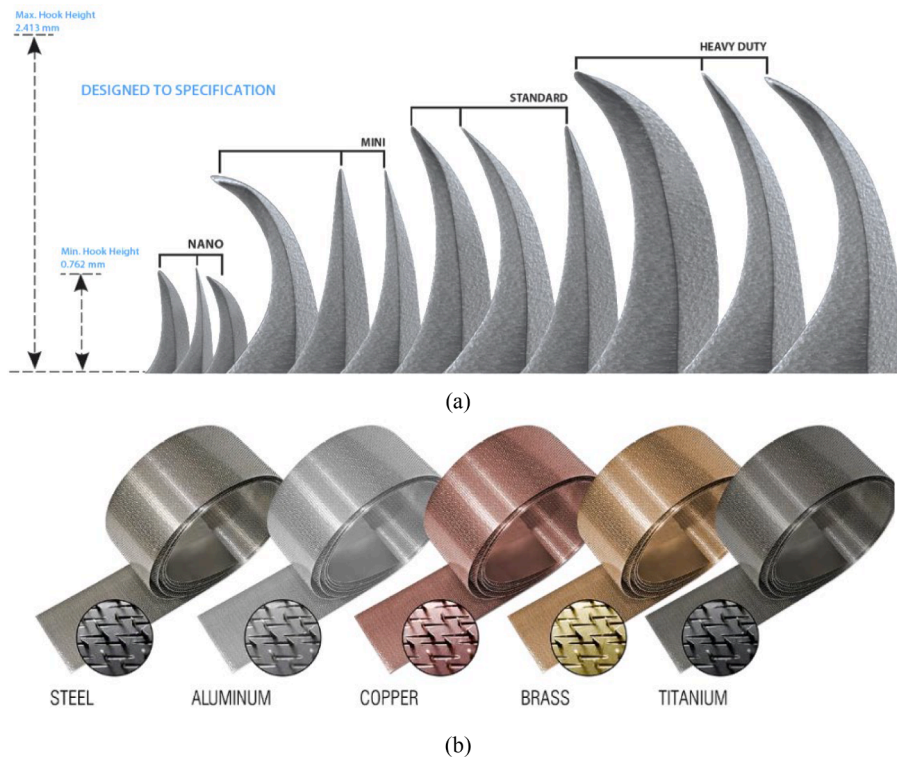


Fig. 1. (a) different hook configuration (b) hooks with different substrate material.

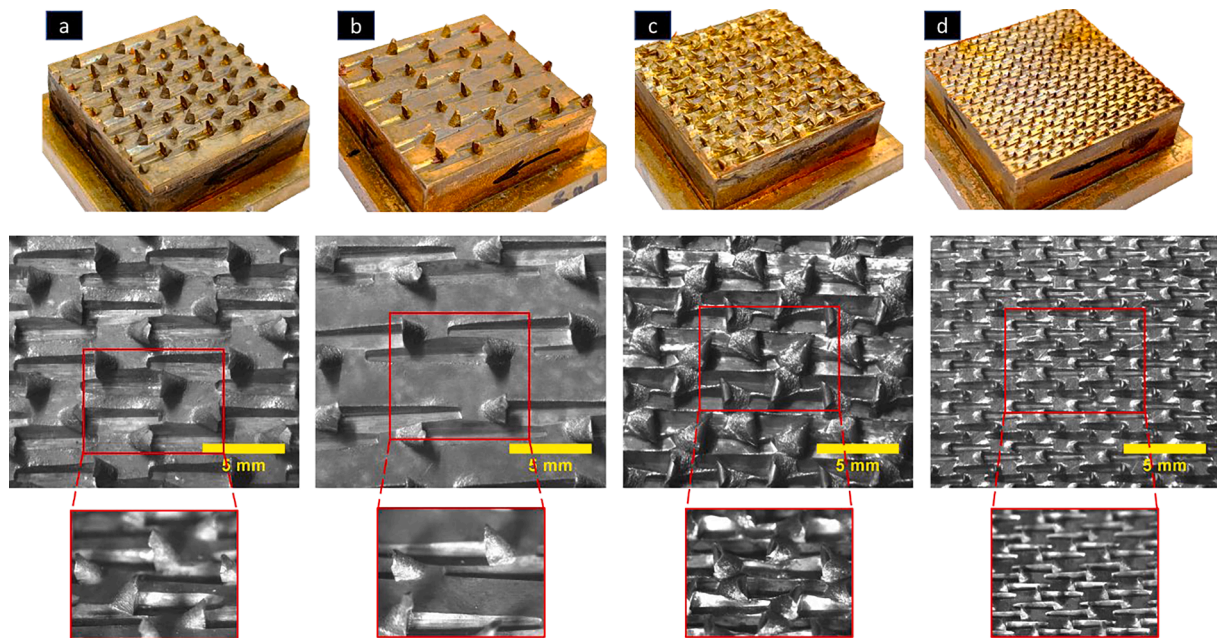


Fig. 2. Tested boiling surfaces: (a) Surface 1 (S1) (b) Surface 2 (S2) (c) Surface 3 (S3) (d) Surface 4 (S4).

skiving manufacturing method has key advantages over other methods, such as its size scalability, mass production, simplicity of design and function, long-term stability, applicability to most metals, resistance to clogging, and low cost.

2. Boiling samples preparation

NUCAP Energy [40] has developed a proprietary manufacturing technique for creating high aspect ratio metal features, trademarked as

GRIPMetal, as shown in Fig. 1. These spikes are available in various sizes and gauge depths, depending on the material being processed. The current study aims to employ these features to enhance the rate of pool boiling heat transfer from copper surfaces in microelectronics cooling applications.

Contrary to many traditional techniques, which completely remove the metal chips from the matrix, the present skiving process only partially removes the metal from the substrate, bending the resulting chips upward to form high aspect ratio metal hook-shaped features, as

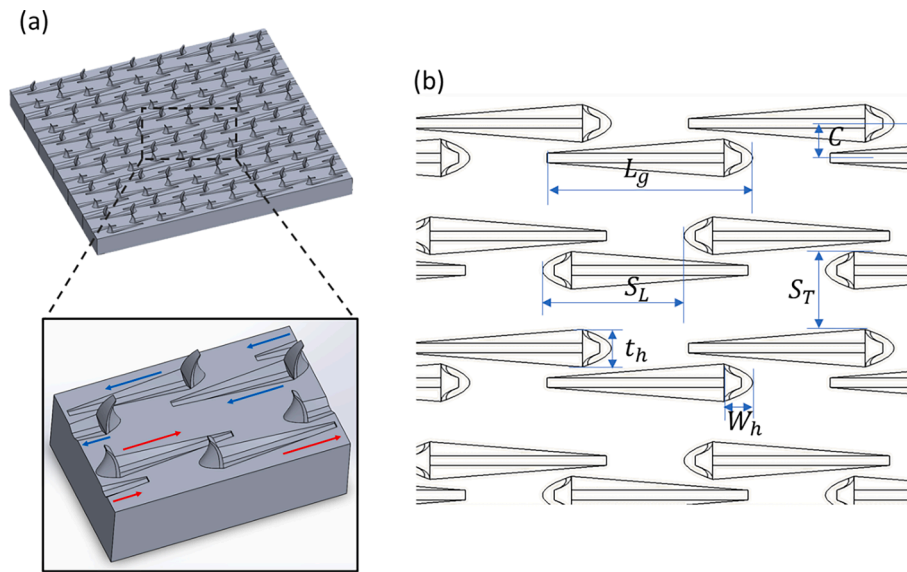


Fig. 3. Description of hook patterns: (a) hook orientation, (b) hook geometrical parameters.

Table 1
Measured geometrical parameters of the examined surfaces.

Surface	Hook Height (H_h)	Hook Shape (Fig. 1)	Streamwise Spacing (S_L)	Spanwise Spacing (S_T)	Width (W_h)	thickness (t_h)	Clearance (C)	Groove Length (L_G)	A_t/A_{bare}
Surface 1 (S1)	1.52	“Standard”	4.021	1.897	1.322	1.31	1.265	5.049	1.56
Surface 2 (S2)	2.25	“Heavy Duty”	4.999	3.449	1.519	1.35	1.340	7.375	1.35
Surface 3 (S3)	1.00	“Mini”	2.968	1.408	1.523	1.43	0.959	4.667	1.80
Surface 4 (S4)	0.63	“Nano”	1.879	0.715	0.419	0.52	0.472	2.403	1.53

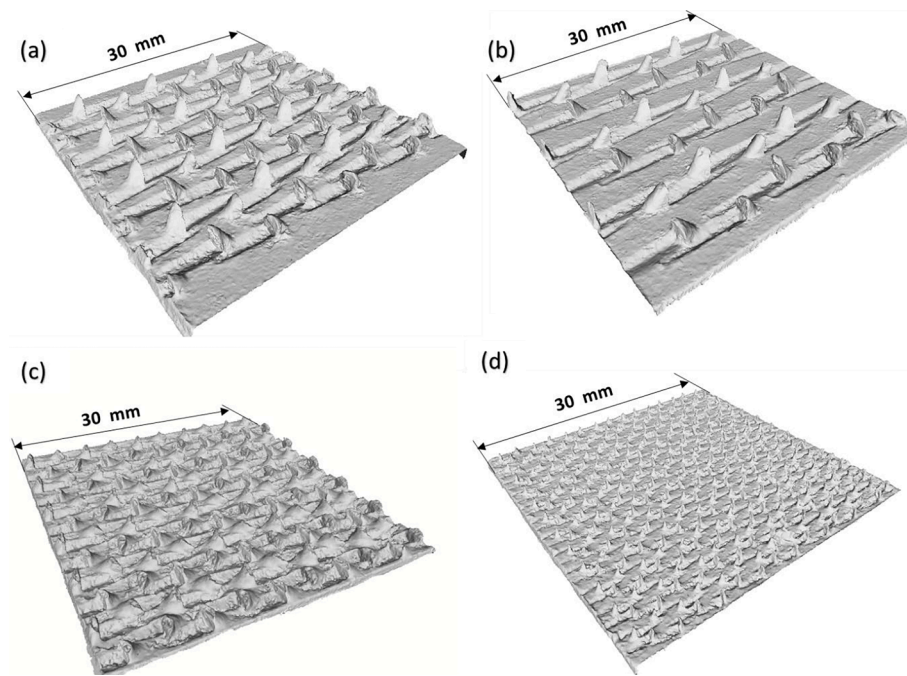


Fig. 4. 3D scan of boiling surfaces (a) Surface 1 (S1) (b) Surface 2 (S2) (c) Surface 3 (S3) (d) Surface 4 (S4).

shown in Fig. 1a. Each hook leaves a groove behind it in the surface, representing its approximate negative volume, as shown in Fig. 1b and Fig. 2. Depending on the tooling and fabrication parameters used (e.g.,

force, material, angle of attack of the tool, tool spacing, etc.), different hook configurations can be generated, which are commercially referred to as “nano,” “mini,” “standard,” and “heavy duty,” as shown in Fig. 1

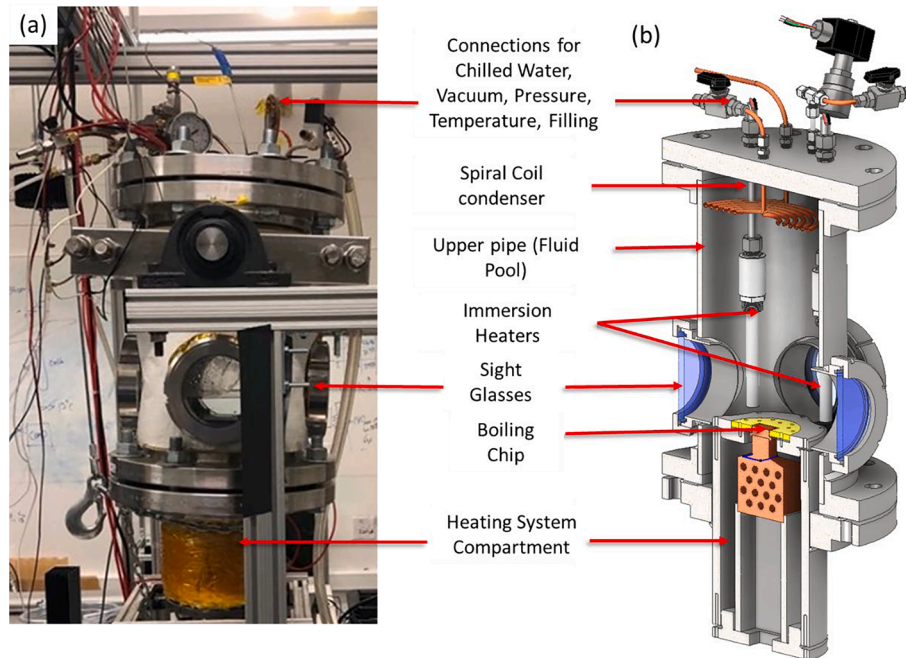


Fig. 5. Experimental boiling facility: (a) photograph of device, (b) half-section diagram.

[40]. The main difference between these configurations is the hook size, which ranges from 0.76 mm to 2.43 mm in height.

In this study, four surfaces with different hook sizes were prepared; these are hereafter referred to as *Surface 1 (S1)*, *Surface 2 (S2)*, *Surface 3 (S3)*, and *Surface 4 (S4)*, as shown in Fig. 2. Microscopic photos in Fig. 2 were captured using a Leica MZ10 F stereo microscope (Leica Microsystems GmbH, Wetzlar, Germany). Each surface had a staggered pattern of hooks with a repeating unit cell, imposed by the manufacturing process parameters and constraints, as shown in Fig. 3 (inset), in which the hooks and groove direction alternate with rows. In other words, the groove location relative to the hooks varies every-two rows (see the difference between the red and blue arrows). The alternating hook directions is a manufacturing constraint of this technology. As shown in Fig. 3, six geometrical parameters were used to describe the hooked surface: groove length, L_g , hook height, H_h , hook thickness, t_h , hook base width, W_h , the clearance between hooks with the same direction, C_h , the streamwise spacing, S_L , and the spanwise spacing between the hooks with opposite directions, S_T . These parameters were measured from microscopic photos at multiple locations for all the surfaces using ImageJ software and are given in Table 1.

Prior to applying the hooks to the surfaces, all the surfaces were ground and polished to achieve the same roughness and ensure that any performance difference originated only from the hook geometry. For better comparison, two bare surfaces were also prepared and polished using the same polishing procedure. The resulting roughness for bare surfaces was about 232.2 nm. The contact angles were measured for the bare surface at several locations using KRUS device (Model DSA100E). The static contact angle was $80^\circ \pm 5.6^\circ$, while the receding and advancing angles were 21.9° , and 102.6° respectively.

The surface area increase offered by the hooks and grooves is a critical factor in enhancing the heat transfer rate. Therefore, the surface area of the samples was measured using the photogrammetry technique. This method depends on extracting a 3D model by capturing several overlapping images of the object from different angles. This was implemented by setting up a studio shooting tent/lightbox that included a turntable that accommodated the scanned part. To overcome the reflective issue of the copper surface, no flash was used, and the system was equipped with a diffused LED light. Matte black background cloth was used for easier recognition of the part by the software. The subject

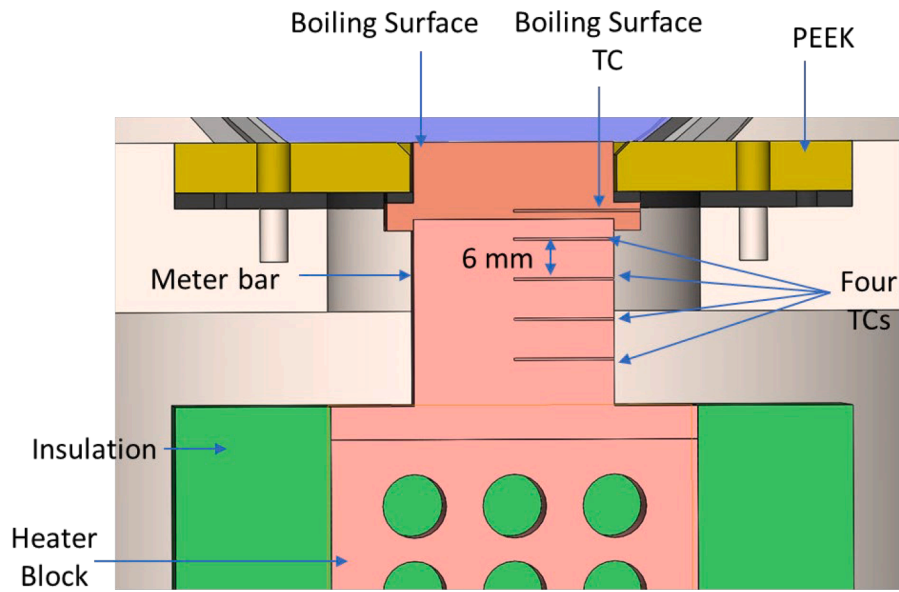
was rotated on a turntable at slow increments of approximately 7° ; each rotation was equal to a camera shot. A Canon EOS 4000D camera was used to capture around 50 shots of each surface. A single shot was taken without the subject but including cloth for the masking step in the reconstruction software. All the images were loaded into Metashape software for reconstruction purposes. Finally, the resulting mesh file was imported into Blender software, where it was adequately aligned in world space and scaled to match the required top surface area of 30 X 30 mm. Fig. 4 shows photos of the final generated 3D-scanned hook-shaped surfaces. It was found that the surface increase ranged from a factor of 1.35 to 1.8 to that of the flat surface. S3 with the medium hook size of 1 mm showed the highest area increase; this was because of the large hook size and their concentrated density over the surface.

3. Experimental apparatus and methodology

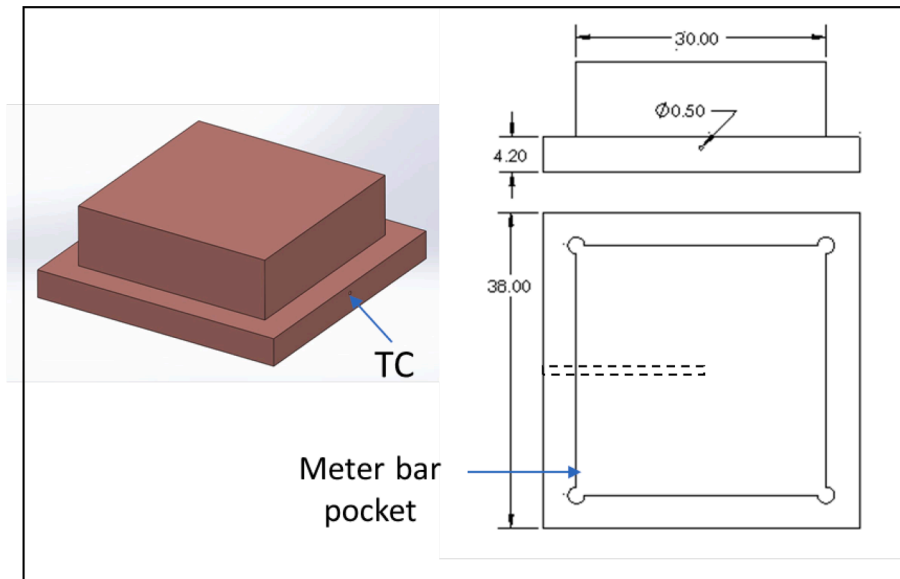
Fig. 5 shows a photograph and cross-section of the pool boiling apparatus used in the current work. This briefly encompasses: (i) the working fluid chamber, (ii) the main boiling surface and its relevant heating and measurement systems, and (iii) the condensation recuperation unit.

3.1. Boiling chamber

The boiling chamber was manufactured from stainless steel pipe (Sch. 40) with an inner diameter of 202.7 mm and length of 457.2 mm with four embedded sight glass panels with a diameter of 100 mm to permit the visualization of the bubble dynamics. A 1 kW compact immersion auxiliary heater with a diameter of 15.8 mm and a length of 123.8 mm was employed to control the working fluid temperature and compensate for the heat loss from the chamber body. The top lid of the chamber was also made of stainless steel and accommodated the condenser inlet and outlet, the filling valve, two solenoid valves, and the pressure and temperature safety and monitoring equipment. One solenoid valve was connected to a compressed air source (3 bars), and the other was connected to a vacuum pump (Vacuubrand MZ 2C NT + 2AK) for control purposes. The chamber was insulated with fiberglass to mitigate heat loss and decrease the required auxiliary heater load.



(a)



(b)

Fig. 6. (a) Cross-section of heating system, (b) boiling surface design.

Table 2

The uncertainties associated with all input variables.

Parameter	Uncertainty
Boiling surface area, A	$3.5 \times 10^{-5} \text{ (m}^2\text{)}$
Thermocouples, T	$\pm 0.2 \text{ K}$
Copper thermal conductivity	$\pm 2\%$ of the nominal value
Thermocouple position, Δx	$\pm 5\%$ of the hole diameter

3.2. Heating system

Fig. 6 shows a detailed section view of the heating system, which is composed of a stack of five components clamped together and confined in a SS pipe 152.4 mm in diameter. These components comprise the (i) interchangeable boiling surface, (ii) heat flux meter bar, (iii) meter bar

support, (iv) PEEK (polyether ether ketone) insert, and (v) the pipe flanges. The boiling chip was fabricated from an oxygen-free copper block with a thermal conductivity of 390 W/mK and a square upper surface width of 30 mm. The chip had a small lateral extension to accommodate a high-temperature silicone gasket which sealed it against the PEEK insert. The boiling chip was clamped against an insulative high-temperature PEEK insert in order to drive the heat flow axially and induce the nucleation only from the chip top surface. The input heat was supplied to the boiling chip through another copper block with 14 embedded 400 W cartridge heaters (9.5 mm in diameter and 50 mm long). This block converges in a square section of 30 mm \times 30 mm \times 40 mm long to intensify the heat flux and serve as a heat flux meter bar to measure the input thermal power to the surface. The boiling chip included a 1.5 mm deep pocket to facilitate easy attachment to the meter bar. The heat flux was calculated by measuring the thermal gradient of the meter bar using four K-type thermocouples ($d = 0.5 \text{ mm}$) separated by 6 mm. The wall temperature was extrapolated using the measured

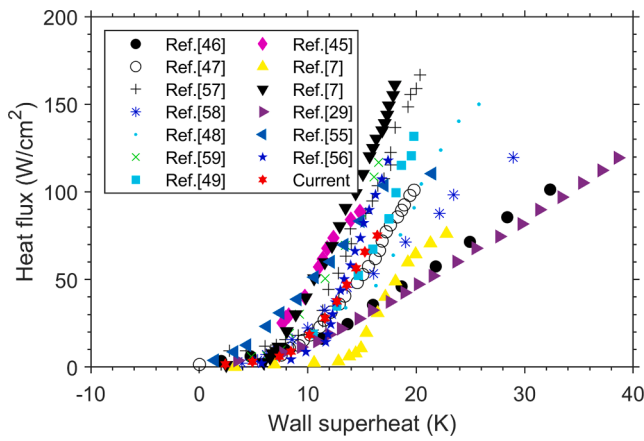


Fig. 7. Comparison of the bare surface with studies from the literature [7,29,45–49,55–59].

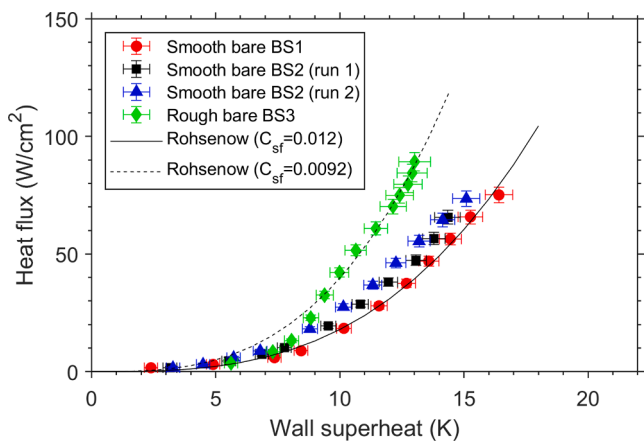


Fig. 8. Repeatability results for the bare surface.

heat flux and measured temperature of the boiling chip at 10.3 mm beneath the boiling surface. To ensure one-dimensional heat flow of the input power, the meter bar and its extension were wrapped with high-temperature ceramic insulation.

3.3. Condenser section

The condenser, shown in Fig. 5, was a spiral coiled copper tube with an outer diameter of 6.35 mm located near the working fluid top lid. It was connected to a controlled water liquid bath to recover the evaporated vapor. The pressure was kept constant at all the heat fluxes by changing the cooling water flow rate through the condenser and using a solenoid valve, whose set point was 0.01 bar above the test pressure. The solenoid valve opened when the condenser response was insufficient, particularly when increasing the input power.

The whole test rig can rotate on a swing mechanism consisting of an aluminum frame, two rotational bearings, and a winch. The fixation frame was thermally insulated from the rig body with thermal breaks made of Garolite G10 which were clamped around the sides of the chamber.

3.4. Instrumentation & data acquisition

The five K-type thermocouples in Fig. 6a were employed throughout the system. The pressure was instrumented using a Gems transducer (connected by T-fitting with the dial gauge). The pressure and temperature measurements were sampled every 2.5 s using an Agilent 34970A data acquisition unit. Electric power to the heaters was provided by two power supplies (Aim TTI, CPX400D) and measured using the power supplies' internal current and voltage measurements. Although the boiling curves were plotted using thermal power measured from the heat flux meter bar, the electric power was used to quantify the thermal efficiency of the whole heating system. It was found that the heating losses ranged from 16 % at low heat fluxes to 5.8 % at high heat fluxes. A MATLAB script was written to control and read data from all devices. To ensure safe operation, an adjustable pressure relief valve was employed. The bubble dynamics were monitored at 2000 FPS utilizing a Phantom high-speed camera (Phantom v4.3) with a 50 mm/F2.0 lens and appropriate lighting through the sight glasses.

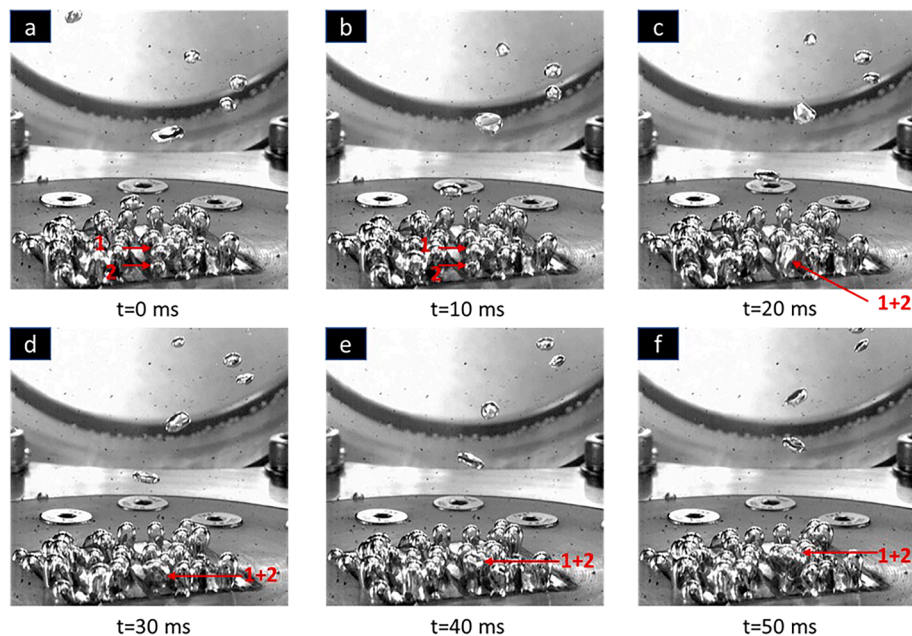


Fig. 9. Bubble behavior at low heat flux of 0.92 W/cm².

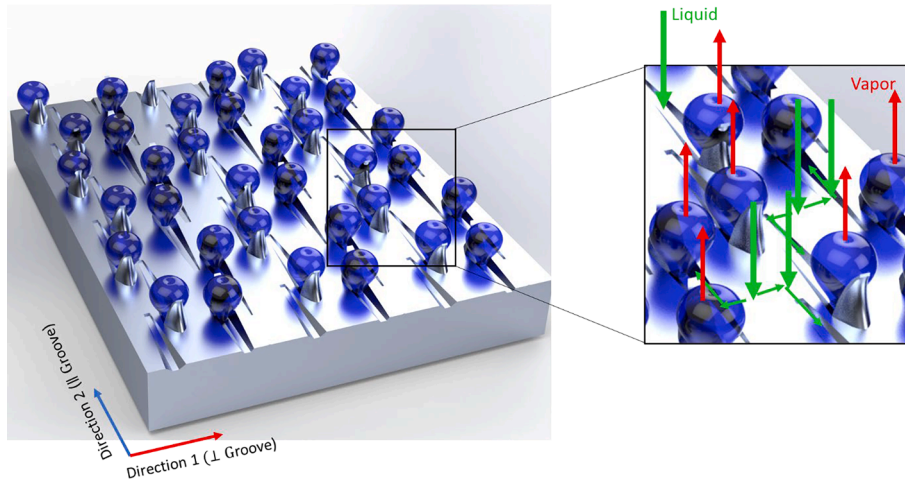


Fig. 10. Working principle of the hook-shaped surface.

3.5. Experimental procedure

For filling, the system was brought to low pressure using the vacuum pump. The pressure difference then caused working fluid to be drawn from the storage tank to the boiling chamber. The pool was filled with approximately-five liters to completely cover the immersion heaters. Prior to testing, non-condensable gases were eliminated by constantly boiling the water and purging of the gases while the chiller was kept off. Under testing conditions, the input heat flux was increased by increments of 3 W/cm^2 until a heat flux of 10 W/cm^2 was reached. Thereafter, the heat flux increment was increased to 10 W/cm^2 until a heat flux of 100 W/cm^2 was reached. Beyond this value, the heat flux increment was decreased to 5 W/cm^2 to precisely detect the CHF. The CHF was identified when the surface temperature exceeded 150 K . Once the CHF was reached, the input power was immediately stopped, and the system pressure was simultaneously increased to 3 bar by the compressed air solenoid valve, immediately causing the vapor film on the boiling surface to condense and bringing the system back to the nucleation regime. This procedure allows fast, safe removal of residual heat from the copper block and the meter bar. The quasi-steady-state conditions were identified at each power when the maximum averaged slope of all recorded temperatures was less than 0.003 K/S over 18 min . All tests were performed with deionized water at saturation at a pressure of 1 atm .

3.6. Data reduction & uncertainty analysis

Upon reaching quasi-steady conditions, the heat flux was evaluated thermally by measuring the temperature gradient in the copper meter bar, as given by the following equation:

$$q'' = -k_b \frac{dT}{dx} \quad (1)$$

where, k_b is meter bar conductivity, and dT/dx is the generated temperature gradient inside the bar.

$$T_s = T_m - \frac{q'' \Delta z}{k_s} \quad (2)$$

$$HTC = \frac{q''}{T_s - T_{sat}} \quad (3)$$

where, T_m is the boiling surface temperature recorded at 10.3 mm beneath the boiling surface, while T_{sat} is the working fluid saturation temperature, measured using a T -type thermocouple.

All thermocouples were calibrated against each other using 303 K to 573 K , resulting in an uncertainty of 0.2 K , as shown in Table 2.

Thereafter, the combined uncertainty in measuring the HTC was determined using the error propagation method described in [41]. This technique was applied to HTC as follows

$$U_h = \sqrt{\left(\frac{\partial h}{\partial q''} U_{q''}\right)^2 + \left(\frac{\partial h}{\partial T_s} U_{T_s}\right)^2 + \left(\frac{\partial h}{\partial T_{sat}} U_{T_{sat}}\right)^2} \quad (4)$$

where U_i is the uncertainty for the quantity i .

The uncertainty in the temperature gradient, dT/dx , was evaluated using the Monte Carlo method used in [42,43]. This method assumes an uncertainty window for each thermocouple reading, bounded by the uncertainties in both temperature and position. Then, a multitude of possible linear trend lines can be determined by randomly moving the temperature readings within their respective windows. The output uncertainty of the temperature gradient can be calculated through the standard deviation of the many slopes found in the previous step. The total uncertainty was approximately 17% for both heat flux and HTC at low heat flux and dropped to less than 6% beyond a heat flux of 10 W/cm^2 .

4. Results & discussion

Experiments were performed to analyze the overall pool boiling heat transfer of the hooked microstructures and to study their boiling activity. The results section begins with a description of the validation of the boiling facility by comparing the performance of the bare surface with the Rohsenow correlation and with many studies from the literature. Next, the main working principle of the proposed structure is discussed by analyzing the bubble behavior on one of the hooked surfaces. Then, the effects of the hook shape, design, and geometry on both HTC and CHF were investigated. Finally, activity/dynamics of the bubbles were compared across all surfaces to qualitatively evaluate the boiling process and build a hypothetical approach to the heat transfer mechanism.

4.1. Bare surface validation

The boiling facility was validated by testing two smooth bare surfaces and comparing their boiling performance with the popular Rohsenow correlation and other studies from the literature [9,44–46] (see Fig. 7 and Fig. 8). Both surfaces were prepared using the same polishing procedure (described above) and resulted in a close average roughness (232.2 nm and 255 nm). As shown in Fig. 7, a huge discrepancy already exists between the results reported in other studies for bare surfaces, which can be attributed to differences in numerous factors, such as surface roughness, contact angle, and surface aging. The current results align well with the results of Kwark et al. [47], Shi et al. [48], and

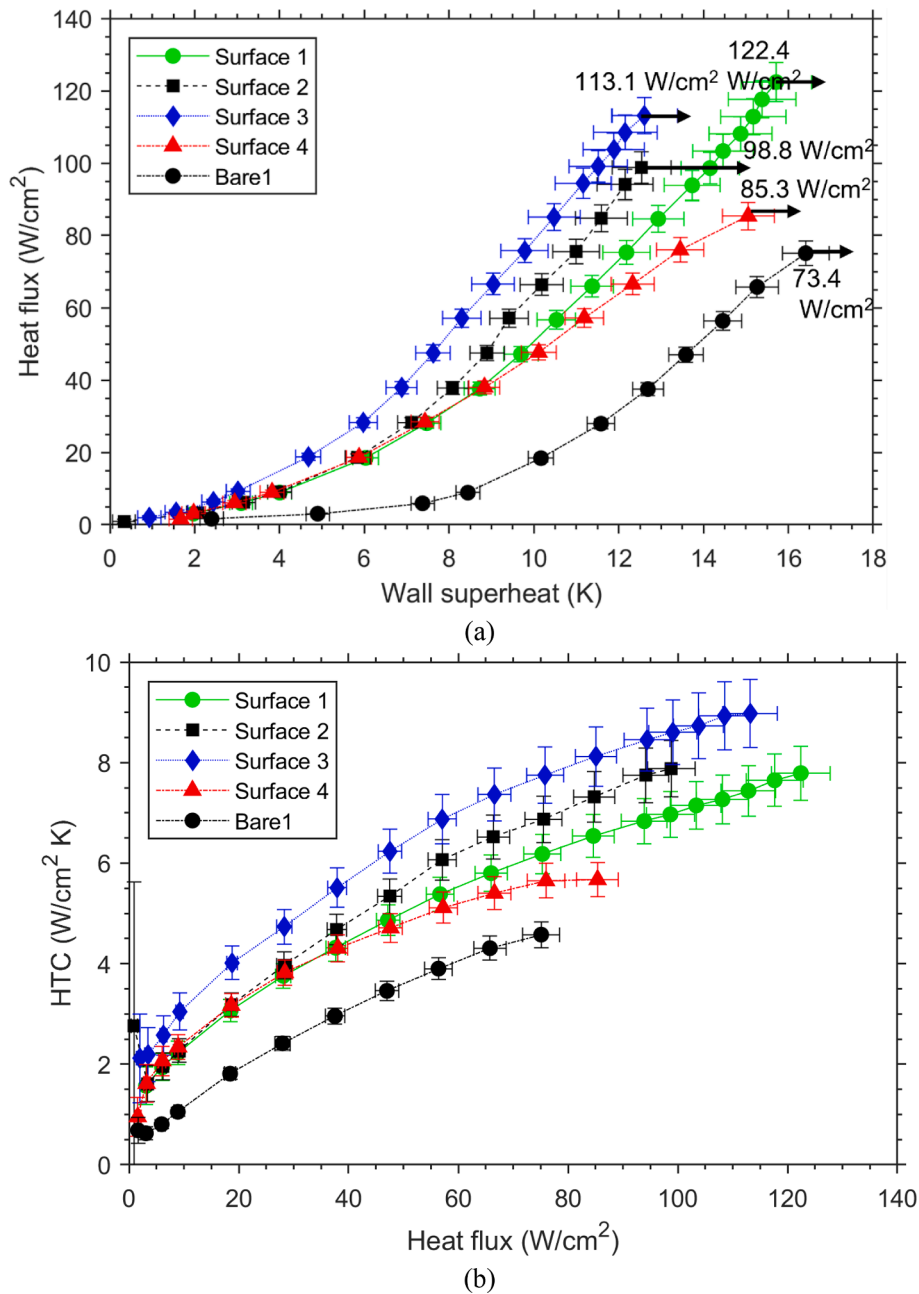


Fig. 11. Comparison between the performance for all surfaces: (a) boiling curve, (b) HTC.

Jaikumar and Kandlikar [49]. However, none of these studies mentioned the roughness of the tested surfaces. Interestingly, the bare surfaces from our results are very close to the Rohsenow correlation at surface-fluid constant, C_{sf} , of 0.012, which agrees well with the value of 0.013 reported by Lienhard [50].

Despite having a good agreement with the HTC, the obtained CHF of $73.4 W/cm^2$ is low compared with other studies and the Zuber correlation. The CHF is greatly impacted by the heater size [51,52], contact angle [53], and the surface roughness [7,53]. With respect to size, to achieve the infinite condition, the heater's characteristic dimensionless length should be larger than 20, as described in [51,52]. The heater's dimensionless size is defined as the ratio between the heater length and the capillary length of the working fluid. The heater size in the current study is $30 mm \times 30 mm$, which is relatively large compared with other studies (see Fig. 7); however, the heated surface did not achieve the infinite condition when working with water. As a result, it is expected to

have a lower CHF, and should be around $\sim 0.75 CHF_{Zuber}$ according to the graph presented in [54], which is still higher than the obtained value. With respect to roughness, Kim et al. [7,53] found that decreasing the roughness from $2.36 \mu m$ to $0.041 \mu m$ deteriorated the CHF from $162.5 W/cm^2$ to $77.5 W/cm^2$. This was demonstrated for a relatively small heater size of $10 mm \times 10 mm$. Therefore, the low CHF ($\sim 74 W/cm^2$) measured in the current study is very reasonable given the relatively large and smooth boiling surfaces used as a baseline. Also, another surface with high unidirectional roughness (Ra of $0.337 \mu m$) prepared like Kim et al. [7] was examined and compared with the two smooth surfaces mentioned above, as shown in Fig. 8. The new rough surface reached a CHF near $90 W/cm^2$. This indicates that the CHF is sensitive to roughness and even the roughness configuration, i.e., unidirectional or bidirectional or random. It is worth mentioning that all the hooked surfaces used in the current study were machined and polished before applying the hooks on the same machine used to machine and polish the

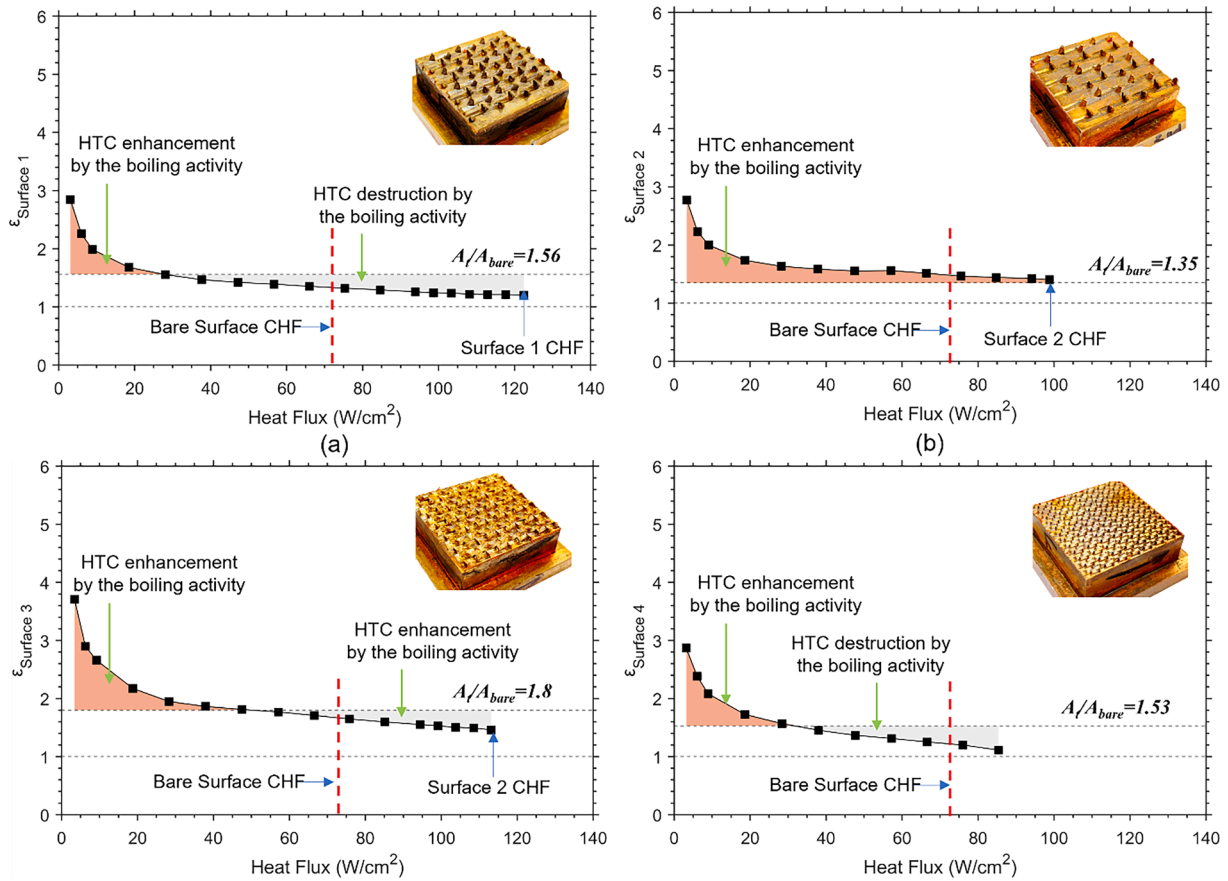


Fig. 12. Heat transfer enhancement ratio for all surface (a) S1, (b) S2, (c) S3, and (d) S4.

Table 3

The HTC and CHF enhancement attained by the proposed surfaces.

	Surface 1	Surface 2	Surface 3	Surface 4
CHF (W/cm^2)	122.41	98.81	113.16	85.33
CHF Enhancement Ratio	1.66	1.33	1.54	1.16
Max HTC Enhancement Ratio	2.84	2.77	3.70	2.87

smooth bare surfaces. Therefore, one of the smooth bare surfaces was used as a baseline surface for comparing the boiling performance of hook surfaces.

Finally, Fig. 8 also shows a very slight difference between the results of both smooth bare surfaces with a difference in wall superheat of less than 1 K, which demonstrates the reproducibility of the results, and the accuracy of this facility.

4.2. Working principle

Typically, roughing the heated boiling surface or adding more artificial cavities helps initiate bubbles faster, enhancing the HTC. We hypothesized that the same behavior would be caused by the grooves created by the GRIPMetal skiving process that forms the hooks. This hypothesis was investigated by visualizing the bubble behavior at a very low heat flux ($\sim 1 \text{ W/cm}^2$) for one of the surfaces (S2 with biggest hook size), as shown in Fig. 9. An organized staggered pattern of bubbles was formed, which followed the hook spacing pattern; this helped confirm the conjecture that these cavities trap the vapor and facilitate the generation of the bubbles. Specifically, the bubbles were formed at the interface line where the hook-shaped fin meets the groove, as shown in Fig. 10. Commonly for bare surfaces, when the wall superheat increases, more bubbles become activated when the trapped vapor bubble sizes

exceed the required critical radius for the bubble to grow. A good feature of the present enhanced surface is that most of the bubbles are activated at once, indicating good repeatability of the manufacturing process of the hooks to produce almost the same size of grooves.

At this low heat flux, the bubbles are discrete and do not disturb or coalesce with each other. Also, no bubbles are formed at the unfinned area of the surface, leaving it wetted and the grooves are fed with replenishing liquid. At very few locations, the bubbles coalesce in the lateral direction (perpendicular to the groove direction), as denoted by the arrows in Fig. 9.

In summary, the hook-groove surfaces functionally enhance boiling heat transfer by (i) increasing the heat transfer area; (ii) creating stable, organized nucleation site patterns which enhance the HTC; and (iii) separating the liquid-vapor phases by leaving a un-nucleating bare surface between the hooks to serve as liquid feeders, which we think can delay the horizontal coalescence and impact the resulting CHF, as discussed below. The effects of changing the hook shape and consequently the groove size and density is discussed in Sec. 4.3.

4.3. Effect of hook geometry

The pool boiling curves for all surfaces at saturation at a pressure of 1 atm are shown in Fig. 11a. The reproducibility of the results for hook surfaces was examined like what was performed for the bare surface in Sec. 4.2, which showed good repeatability with a difference in wall superheat of less than 1.4 K. A significant improvement in the HTC for all surfaces is evident at low and high heat fluxes when compared with the bare surface. All the hooked surfaces immediately initiated nucleation, achieving a much smaller wall superheat (less than 2 K) at the onset of nucleate boiling (ONB), compared with 4 K for the bare surface (evaluated by the slope change of the boiling curve). All surfaces showed

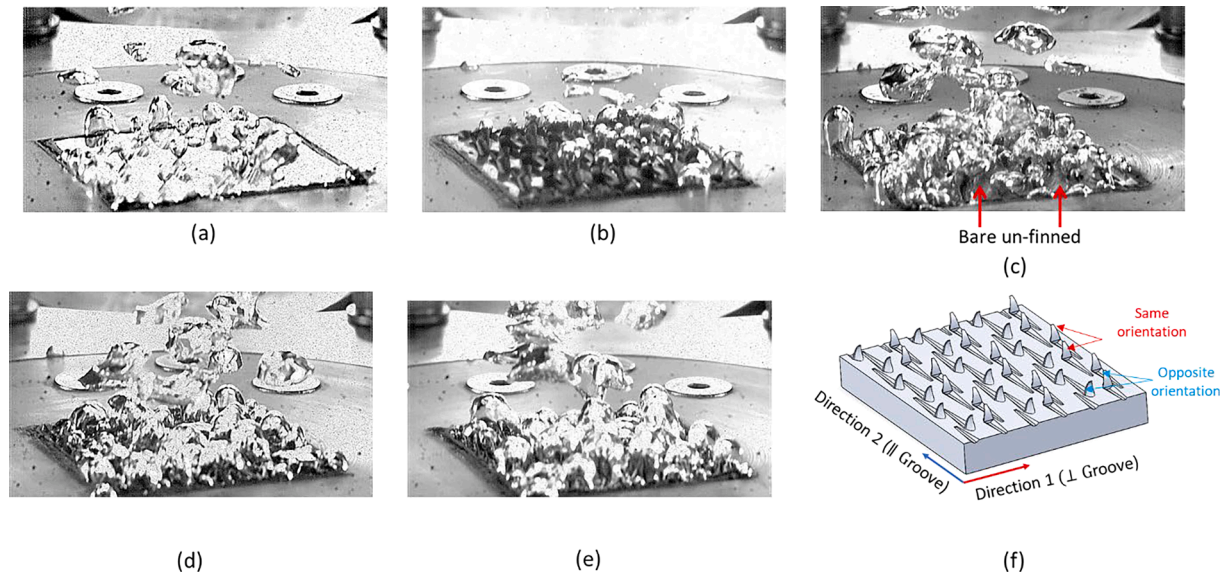


Fig. 13. Comparison between the behavior of the bubbles for all surfaces at a low heat flux of 3.1 W/cm^2 . (a) bare surface, (b) S1, (c) S2, (d) S3, (e) S4, and (f) reference of hook orientation.

monotonic increasing trends for the HTC; the highest HTC achieved was $8.9 \text{ W/cm}^2\text{K}$ at a wall superheat of 12.6 K for S3, as shown in Fig. 11b. At a heat flux of 1.7 W/cm^2 , surfaces S3 and S4 had the lowest wall superheat of 0.92 K and 1.6 K , respectively, with a similar trend to other hook-shaped surfaces; however, beyond a heat flux of 38 W/cm^2 , S4 had a lower slope, achieving a slightly higher CHF of 85.3 W/cm^2 than the bare surface. S1 had a significant CHF enhancement, achieving 122 W/cm^2 compared with 73.4 W/cm^2 for the bare surface (67 % improvement).

For better comparison between the surfaces, a new factor named the enhancement ratio, $\varepsilon = \text{HTC}_{\text{hook}}/\text{HTC}_{\text{bare}}$, was defined and plotted versus the heat flux for all surfaces, as shown in Fig. 12. The heat transfer coefficient for the bare surface, HTC_{bare} , was predicted using the Rohsenow correlation even after the CHF because it offered an excellent agreement with the bare data shown in Fig. 8. Overall, the maximum HTC enhancement ratio value happened at low heat flux for all surfaces and measured 2.84 (S1), 2.77 (S2), 3.7 (S3), and 2.87 (S4), as summarized in Table 3 (critical heat flux improvements for all surfaces are given in this table).

In Fig. 12, a horizontal line is plotted to represent the area ratio, which distinguishes the enhancement offered by the bubbles' dynamics from the increased surface area offered by the hooks and grooves. Therefore, the two regions can be easily identified: 1) the light orange region above the area ratio line where the boiling activity and surface area collectively cause the HTC enhancement, and 2) the light grey region below where the boiling activity destroys the HTC. However, however, the enhancement ratio, ε , is still higher than 1 since the area enhancement has the dominant positive effect.

At low heat fluxes, the boiling activity positively enhanced the HTC for all surfaces, especially S3, which displayed an enhancement ratio close to 4. It can be observed that the light orange region (enhancement by boiling activity) is almost the same for all surfaces except S3 at fluxes of less than 30 W/cm^2 . This indicates that the hook density is not the only factor that controls the HTC—it is possible that the cavity size formed by the groove plays a role. If the hook density is the main factor enhancing the HTC, we would expect that S4, with the highest density of hooks, would achieve the highest HTC enhancement by boiling activity; however, this did not happen. Since the groove width for S1, S2, and S3 is close (Fig. 2) and much bigger than S4, it is more accurate to say, increasing the hook density (i.e., nucleation sites) at low heat flux exhibits better HTC if the groove size, t_h within $1.3\text{--}1.4 \text{ mm}$ (Table 1).

At high heat fluxes, the boiling activity had a detrimental effect on the HTC and worked against the area enhancement ratio (S1, S3, and S4), except for S2, which exhibited a positive enhancement by boiling activity of its HTC at the whole range of the tested heat fluxes until 1 hitting reaching the CHF. The main characteristic of S2 is that it has the lowest density of hooks and high spanwise spacing between the fins, S_T . This coincides with observations by Masri et al. [60], who found that it is possible to have higher HTC with fewer nucleation sites. They related this phenomenon to postponing the coalescence process between bubbles, which we examined in a visualization study in Sec. 4.4. Higher nucleation sites yield better HTC at low heat flux if the groove size, t_h is within $1.3\text{--}1.4 \text{ mm}$. On the other hand, reducing the nucleation sites with some bare areas in between hooks may not achieve the same enhancement in HTC observed in S3 at low heat fluxes, but it extends the flux range, in which the boiling activity has a positive effect (S2).

With respect to the CHF, comparing S1 and S4 (with almost the same area ratio) show that fewer nucleation sites help increase the CHF. A similar conclusion is seen by comparing S1 and S3. However, this conclusion cannot be generalized because S2 (with the least number of hooks) achieved a CHF of 98.8 W/cm^2 (less than surfaces S1 and S3). Also, Surfaces 1 and 2 have a very similar number of nucleation sites and cavity widths, t_h , leading to almost the same enhancements of HTC at low heat flux. However Surface 1 shows a better CHF because it possesses a larger heat transfer area. Therefore, surfaces with fewer number of hooks and higher area ratios (i.e., optimum spacing between the hooks) result in higher CHF.

In conclusion, three connected parameters are responsible for the boiling performance of hooked surfaces: (i) nucleation site density which affects the left part of the graph, (ii) bare area between the hooks, which affects the right part of the graph, and (iii) the area ratio which affects the whole range. Because changing the hook type changes the other parameters, there is a need to investigate the impact of each parameter separately which will be performed in a future study with only one type of hook.

4.4. Visualization study

To understand the results in Fig. 12, the bubble behavior was captured at low and high heat fluxes, as shown in Fig. 13 to Fig. 15. Fig. 13 shows that the nucleation started for all hook surfaces compared with the bare surface. Only a few bubbles exist on the bare surface. Other

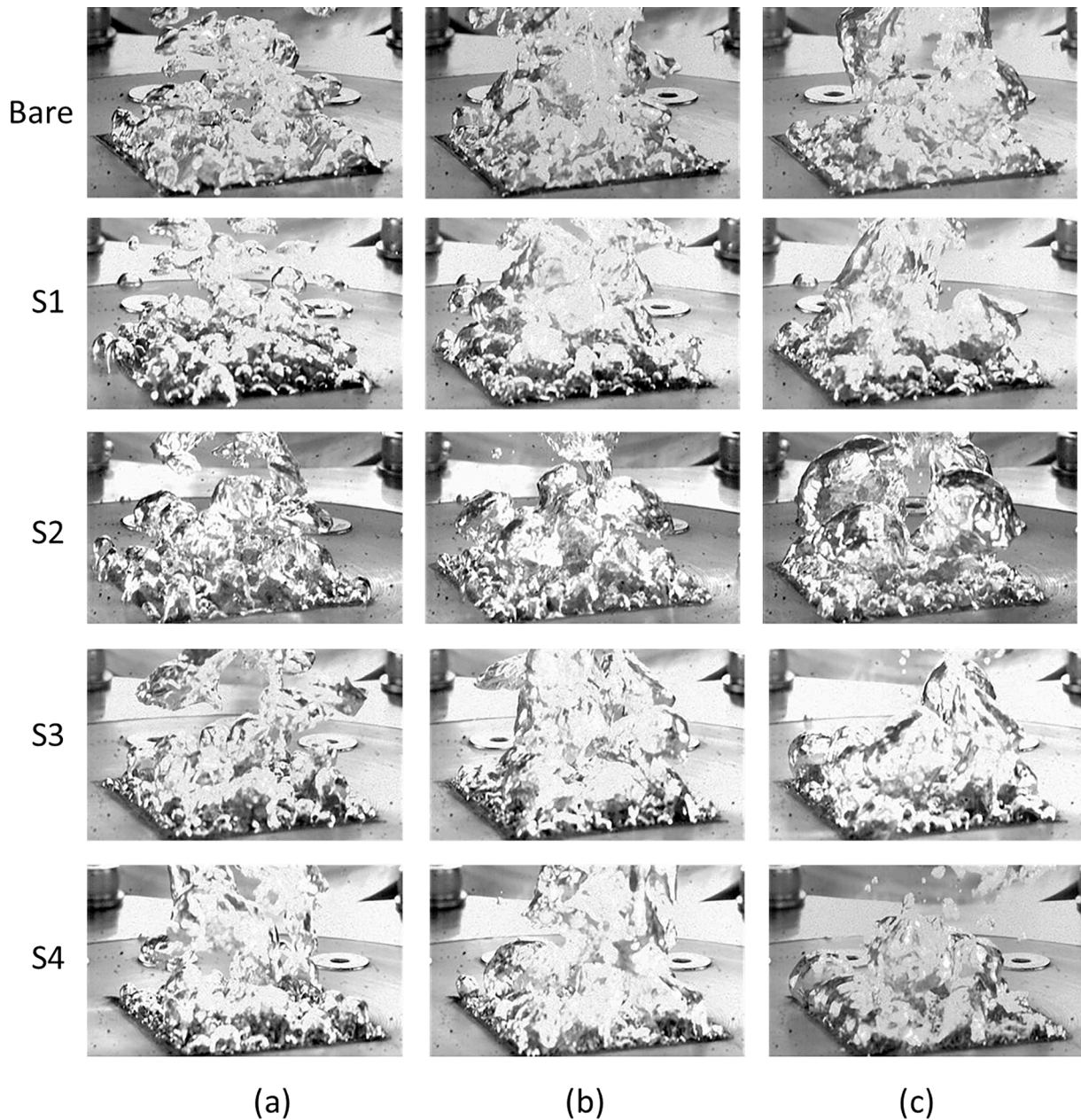


Fig. 14. Comparison of bubble behavior for all surfaces at moderate heat fluxes: (a) $\sim 9 \text{ W/cm}^2$, (b) $\sim 18.5 \text{ W/cm}^2$, and (c) $\sim 28 \text{ W/cm}^2$.

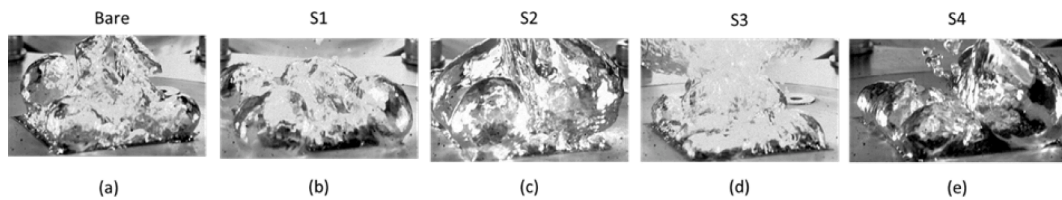


Fig. 15. Comparison of the bubble behavior for all surfaces at high heat fluxes near the CHF: (a) 47 W/cm^2 , (b) 84.5 W/cm^2 , (c) 84.7 W/cm^2 , (d) 85 W/cm^2 and (e) 64.4 W/cm^2 .

bubbles seen in the view of the bare surfaces in Fig. 13a are generated at the edges. S1 had relatively few nucleation sites at this low heat flux, indicating that larger superheat is needed to activate other locations.

By contrast, S2 achieved an almost organized nucleation pattern, with one bubble occupying each groove. At this heat flux, bubble coalescence rarely occurred for this surface and usually happened between

the bubbles created at the hooks with the opposite orientation, as shown explained in Fig. 9. Surfaces 3 and 4 showed an early coalescence between bubbles, resulting in a larger bubble which covered several hook-and-groove features. Consequently, at low heat fluxes up to 5.7 W/cm^2 (Fig. 12), S3 showed the lowest wall superheat, which indicates that hook size (i.e. groove size) controls the ONB while hook density dictates

coalescence at the surface.

As heat flux was increased from Fig. 13 to Fig. 14, the surfaces activated more nucleation sites and induced more bubble coalescence for all surfaces. All surfaces nucleate everywhere except S2 which has some un-finned, non-nucleating areas denoted by red arrows in Fig. 13c. Coalescence happens either at the surface between small bubble seeds or downstream between the departed larger bubbles; this occurs for most of the surfaces at a moderate heat flux as shown in Fig. 14. The big bubbles depart and merge, while other small bubbles are generated at the surface. However, there is a distinction in terms of the extent of coalescence between surfaces S1-S4. Each surface is covered with a different ratio of small and large bubbles. For instance, S1 and S2 exhibited mostly small bubbles everywhere on the surfaces, and the coalescence happens downstream (Fig. 14c). For S3 and S4, the share of large bubbles at the surface is significantly higher than small bubbles (Fig. 14c). In particular, Surface 4 is occupied by several very large and merged mushroom-shaped bubbles at a heat flux of 28 W/cm^2 (Fig. 14c) which we conjecture sped up the coalescence in both directions (streamwise and spanwise) and triggered the CHF (Fig. 15e). Together, these results indicate that hook density (i.e., spanwise, S_T , and streamwise, S_L) is the governing parameter of coalescence.

The CHF was triggered when the high-velocity vapor flow impeded the downward liquid supply. We conjecture that the triggering mechanism for the CHF on the hooked surfaces is related to the available unfinned area on the surface, i.e spanwise, S_T , and streamwise, S_L . The nucleation commonly happens at the groove end near the hook, leaving the rest of the groove and the unfinned area wetted with the liquid, as described in Sec. 4.2. We hypothesize that the groove front works as a liquid artery and supplies the nucleation sites with the required sub-cooled liquid either from above or from the unified space, as shown in Fig. 10 (inset).

Coalescence starts between the adjacent hooks with the opposite orientation (perpendicular to groove direction shown in Fig. 13f), since S_T is smaller than S_L for all surfaces, as discussed above in Sec. 4.2. We think that the CHF is triggered at the moment the coalescence happens in both directions, filling the unfinned area with a big bubble. Another possibility is that the bubble formation on the unfinned area is due to the high wall superheat; this facilitates the lateral coalescence between the bubbles. As a result, the liquid movement through the groove front and the unfinned area is disturbed, triggering the CHF. This supports the observation found in Sec. 4.3, that the surface with highest area ratio (A_f/A_{bare}) and fewest number of hooks (large S_T , and S_L) is better with respect to the CHF. Therefore, S1 and S3 had the highest CHF, as the available unfinned area per grooves is relatively large compared to the low hook density of these surfaces. S3 had a minimally unfinned area, but still some parts of the grooves were wetted and not nucleating. This also explains the issue experienced by S4, which had the smallest hook size and the highest hook density. Because the unfinned area is minimal, and the grooves are very close to each other, a fast transition between the boiling regime occurred.

5. Summary & conclusions

A unique skiving process was used to create robust, low-cost, high-aspect-ratio hook-shaped fins (GRIPMetal) to enhance the pool boiling heat transfer rate for immersion cooling heat sinks for electronic components. The hook manufacturing leaves a groove in the substrate, representing its approximate negative volume. A bare benchmark surface and four copper surfaces with different sizes, densities, and shapes of hooks were fabricated. Experiments were performed with water as the working fluid at saturation conditions. All surfaces were tested horizontally and upward facing at a pressure of 1 atm. The main outcome and conclusions are summarized as follows:

- Overall, the surfaces with integrated hooks improved the boiling heat transfer coefficient and increased the CHF significantly

compared with the bare surface. This is attributed to the additional surface area offered by the hook-shaped fins and their corresponding grooves, superior nucleation site density, and assisted liquid wicking through the front of the grooves.

- S3, with a medium hook size (1 mm), showed the maximum HTC of $8.9 \text{ W/cm}^2\text{K}$, representing 96 % enhancement compared with the maximum HTC achieved by the bare surface. A significant portion of this enhancement relates to the additional surface area offered by the hook shape and specific area of these surfaces. The total surface area of the developed hooked surfaces was measured using the photogrammetry technique; S3 was approximately 1.8 times higher than the flat surface. The other contribution to enhancement came from the increase in density of the nucleation sites.
- S1, with a hook size of 1.52 mm, achieved a significant increase in CHF of 122 W/cm^2 , which is a factor of about 1.6 greater than the bare surface. We propose that available non-nucleating parts of the grooves and the unfinned area of the surface are reasons for the delay in reaching CHF. Bubbles nucleated at the interface between the hook and the groove, leaving the rest of the groove and the unfinned area wetted and the nucleation sites fed. This only happened for surfaces with big hook sizes and high hook density (S1 and S2).
- For higher hook densities and smaller hook sizes, it was found that large bubbles occupied several hooks and grooves. This sped the lateral coalescence of the bubbles at the surface, leading to a fast transition between the boiling regime and the CHF being triggered very early. This occurred for S4, which had the smallest hook size (0.6 mm) and the highest hook density, and S4 achieved a CHF of 85.3 W/cm^2 , which is slightly lower than that of the baseline surface.

The current study has shown that, with a strategic distribution of the hooks on the boiling surface, simultaneous enhancement of the HTC and CHF can be achieved. These surfaces can be implemented in advanced two-phase cooling systems, such as thermosyphons, immersion coolers, and vapor chambers; this impacts many industries including but not limited to electronics cooling, aerospace, and telecommunications.

The next step of this work is to study the bubble departure properties of GRIPMetal hooked surfaces and to examine the boiling enhancement offered at different orientations to simulate operating conditions similar to many practical immersion cooling systems.

Declaration of Competing Interest

The authors declare that they have no known competing financial interests or personal relationships that could have appeared to influence the work reported in this paper.

Acknowledgements

The authors gratefully acknowledge the support of the Natural Sciences and Engineering Research Council of Canada (NSERC) grant ALLRP 552123-20.

References

- [1] A. Ali, Thermal performance and stress analysis of heat spreaders for immersion cooling applications, *Appl. Therm. Eng.* 181 (2020), 115984, <https://doi.org/10.1016/j.applthermaleng.2020.115984>.
- [2] P. Chen, S. Harmand, S. Ouenzerfi, Immersion cooling effect of dielectric liquid and self-wetting fluid on smooth and porous surface, *Appl. Therm. Eng.* 180 (2020), 115862, <https://doi.org/10.1016/j.applthermaleng.2020.115862>.
- [3] X. Wang, B. Li, D. Gerada, K. Huang, I. Stone, S. Worrall, Y. Yan, A critical review on thermal management technologies for motors in electric cars, *Appl. Therm. Eng.* 201 (2022), <https://doi.org/10.1016/j.applthermaleng.2021.117758>.
- [4] M.A. Chan, C.R. Yap, K.C. Ng, Pool boiling heat transfer of water on finned surfaces at near vacuum pressures, *J. Heat Transf.* 132 (2010) 1–6, <https://doi.org/10.1115/1.4000054>.
- [5] K.N. Rainey, S.M. You, Pool boiling heat transfer from plain and microporous, square pin-finned surfaces in saturated FC-72, *J. Heat Transfer.* 122 (2000) 509–516, <https://doi.org/10.1115/1.1288708>.

- [6] D. Zhong, J. Meng, Z. Li, Saturated pool boiling from downward facing structured surfaces with grooves, *Huagong Xuebao/CIESC J.* 67 (2016) 3559–3565, <https://doi.org/10.11949/j.issn.0438-1157.20160015>.
- [7] J. Kim, S. Jun, R. Lakshminarayanan, S.M. You, Effect of surface roughness on pool boiling heat transfer at a heated surface having moderate wettability, *Int. J. Heat Mass Transf.* 101 (2016) 992–1002, <https://doi.org/10.1016/j.ijheatmasstransfer.2016.05.067>.
- [8] A. Suszko, M.S. El-Genk, Bubbles transient growth in saturation boiling of PF-5060 dielectric liquid on dimpled Cu surfaces, *J. Therm. Sci. Eng. Appl.* 8 (2016), 021016, <https://doi.org/10.1115/1.4032367>.
- [9] A.K. Das, P.K. Das, P. Saha, Nucleate boiling of water from plain and structured surfaces, *Exp. Therm. Fluid Sci.* 31 (2007) 967–977, <https://doi.org/10.1016/j.expthermflusci.2006.10.006>.
- [10] K. Zhang, L. Bai, H. Jin, G. Lin, G. Yao, D. Wen, A comparative study of pool boiling heat transfer in different porous artery structures, *Appl. Therm. Eng.* 202 (2022), 117759, <https://doi.org/10.1016/j.applthermaleng.2021.117759>.
- [11] Y. Nasersharifi, M. Kaviany, G. Hwang, Pool-boiling enhancement using multilevel modulated wick, *Appl. Therm. Eng.* 137 (2018) 268–276, <https://doi.org/10.1016/j.applthermaleng.2018.03.073>.
- [12] K.H. Chu, Y.S. Joung, R. Enright, C.R. Buie, E.N. Wang, Hierarchically structured surfaces for boiling critical heat flux enhancement, *Appl. Phys. Lett.* 102 (2013), <https://doi.org/10.1063/1.4801811>.
- [13] C.M. Patil, S.G. Kandlikar, Pool boiling enhancement through microporous coatings selectively electrodeposited on fin tops of open microchannels, *Int. J. Heat Mass Transf.* 79 (2014) 816–828, <https://doi.org/10.1016/j.ijheatmasstransfer.2014.08.063>.
- [14] C.-H. Choi, M. David, Z. Gao, A. Chang, M. Allen, H. Wang, C. Chang, Large-scale generation of patterned bubble arrays on printed Bi-functional boiling surfaces, *Sci. Rep.* 6 (2016) 23760, <https://doi.org/10.1038/srep23760>.
- [15] C.S. Sujith Kumar, Y.W. Chang, P.H. Chen, Effect of heterogeneous wettable structures on pool boiling performance of cylindrical copper surfaces, *Appl. Therm. Eng.* 127 (2017) 1184–1193, <https://doi.org/10.1016/j.applthermaleng.2017.08.069>.
- [16] P.J. Berenson, Experiments on pool-boiling heat transfer, *Int. J. Heat Mass Transf.* 5 (1962) 985–999, [https://doi.org/10.1016/0017-9310\(62\)90079-0](https://doi.org/10.1016/0017-9310(62)90079-0).
- [17] M.M. Rahman, E. Ölceroğlu, M. McCarthy, Scalable nanomanufacturing of virus-templated coatings for enhanced boiling, *Adv. Mater. Interfaces.* 1 (2014) 1–6, <https://doi.org/10.1002/admi.201300107>.
- [18] G. Liang, I. Mudawar, Review of pool boiling enhancement by surface modification, *Int. J. Heat Mass Transf.* 128 (2019) 892–933, <https://doi.org/10.1016/j.ijheatmasstransfer.2018.09.026>.
- [19] N. Tran, U. Sajjad, R. Lin, C.C. Wang, Effects of surface inclination and type of surface roughness on the nucleate boiling heat transfer performance of HFE-7200 dielectric fluid, *Int. J. Heat Mass Transf.* 147 (2020), 119015, <https://doi.org/10.1016/j.ijheatmasstransfer.2019.119015>.
- [20] U. Sajjad, I. Hussain, K. Hamid, S.A. Bhat, H.M. Ali, C.C. Wang, A deep learning method for estimating the boiling heat transfer coefficient of porous surfaces, *J. Therm. Anal. Calorim.* (2021), <https://doi.org/10.1007/s10973-021-10606-8>.
- [21] A. Elkholy, R. Kempers, Enhancement of pool boiling heat transfer using 3D-printed polymer fixtures, *Exp. Therm. Fluid Sci.* 114 (2020), 110056, <https://doi.org/10.1016/j.expthermflusci.2020.110056>.
- [22] A.K. Das, P.K. Das, P. Saha, Performance of different structured surfaces in nucleate pool boiling, *Appl. Therm. Eng.* 29 (2009) 3643–3653, <https://doi.org/10.1016/j.applthermaleng.2009.06.020>.
- [23] W. Nakayama, T. Daikoku, H. Kuwahara, T. Nakajima, Dynamic model of enhanced boiling heat transfer on porous surfaces: Part II: Analytical modeling, *J. Heat Transfer.* 102 (1980) 451–456, <https://doi.org/10.1115/1.3244321>.
- [24] K. Stephan, J. Mitrovic, Heat transfer in natural convective boiling of refrigerants and refrigerant-oil mixtures in bundles of T-shaped finned tubes, *Am. Soc. Mech. Eng.* (1981) 131–146.
- [25] T. Ma, X. Liu, J. Wu, H. Li, Effects of geometrical shapes and parameters of reentrant grooves on nucleate pool boiling heat transfer from porous surfaces, in: *Int. Heat Transf. Conf. Digit. Libr.*, Begel House Inc., 1986.
- [26] L.H. Chien, R.L. Webb, A parametric study of nucleate boiling on structured surfaces part II: Effect of pore diameter and pore pitch, *Am. Soc. Mech. Eng. Heat Transf. Div. HTD.* 326 (1996) 137–143.
- [27] S. Zhang, Y. Tang, J. Zeng, W. Yuan, J. Chen, C. Chen, Pool boiling heat transfer enhancement by porous interconnected microchannel nets at different liquid subcooling, *Appl. Therm. Eng.* 93 (2016) 1135–1144, <https://doi.org/10.1016/j.applthermaleng.2015.10.044>.
- [28] D. Deng, W. Wan, J. Feng, Q. Huang, Y. Qin, Y. Xie, Comparative experimental study on pool boiling performance of porous coating and solid structures with reentrant channels, *Appl. Therm. Eng.* 107 (2016) 420–430, <https://doi.org/10.1016/j.applthermaleng.2016.06.172>.
- [29] Y. Sun, G. Chen, S. Zhang, Y. Tang, J. Zeng, W. Yuan, Pool boiling performance and bubble dynamics on microgrooved surfaces with reentrant cavities, *Appl. Therm. Eng.* 125 (2017) 432–442, <https://doi.org/10.1016/j.applthermaleng.2017.07.044>.
- [30] W. Hao, T. Wang, Y. Yan Jiang, C. Guo, C. Hong Guo, Pool boiling heat transfer on deformable structures made of shape-memory-alloys, *Int. J. Heat Mass Transf.* 112 (2017) 236–247, doi: 10.1016/j.ijheatmasstransfer.2017.04.113.
- [31] P.J. Marto, L.V.J. Lepere, Pool boiling heat transfer from enhanced surfaces to dielectric fluids, *J. Heat Transfer.* 104 (1982) 292–299, <https://doi.org/10.1115/1.3245086>.
- [32] L.H. Chien, R.L. Webb, Visualization of pool boiling on enhanced surfaces, *Exp. Therm. Fluid Sci.* 16 (1998) 332–341, [https://doi.org/10.1016/S0894-1777\(97\)10032-2](https://doi.org/10.1016/S0894-1777(97)10032-2).
- [33] A.E. Bergles, Max Jakob memorial award lecture heat transfer enhancement — the encouragement and accommodation of high heat fluxes, *J. Heat Transfer.* 119 (1997) 8–19.
- [34] A. Kumar, C.C. Wang, Nucleate pool boiling heat transfer of R-1234ze(E) and R-134a on GEWA-B5H and smooth tube with the influence of POE oil, *Appl. Therm. Eng.* 201 (2022), 117779, <https://doi.org/10.1016/j.applthermaleng.2021.117779>.
- [35] D. Jafari, W.W. Wits, The utilization of selective laser melting technology on heat transfer devices for thermal energy conversion applications: a review, *Renew. Sustain. Energy Rev.* 91 (2018) 420–442, <https://doi.org/10.1016/j.rser.2018.03.109>.
- [36] A. Hayes, P.A. Raghupathi, T.S. Emery, S.G. Kandlikar, Regulating flow of vapor to enhance pool boiling, *Appl. Therm. Eng.* (2018), <https://doi.org/10.1016/j.applthermaleng.2018.12.091>.
- [37] K.K. Wong, K.C. Leong, Saturated pool boiling enhancement using porous lattice structures produced by Selective Laser Melting, *Int. J. Heat Mass Transf.* 121 (2018) 46–63, <https://doi.org/10.1016/j.ijheatmasstransfer.2017.12.148>.
- [38] C. Zhang, L. Zhang, H. Xu, P. Li, B. Qian, Performance of pool boiling with 3D grid structure manufactured by selective laser melting technique, *Int. J. Heat Mass Transf.* 128 (2019) 570–580, <https://doi.org/10.1016/j.ijheatmasstransfer.2018.09.021>.
- [39] A. Elkholy, Characterization of Heat Exchange for Additively Manufactured Components, York University, 2021.
- [40] Home - NUCAP Energy, n.d. Available from: <<https://www.nucapenergy.com/>> (accessed December 12, 2021).
- [41] S.J. Kline, Describing uncertainty in single sample experiments, *Mech. Eng.* 75 (1953) 3–8.
- [42] R. Kempers, P. Kolodner, A. Lyons, A.J. Robinson, A high-precision apparatus for the characterization of thermal interface materials, *Rev. Sci. Instrum.* 80 (2009), <https://doi.org/10.1063/1.3193715>.
- [43] R. Kempers, A. Robinson, Heated meter bar techniques: what you should know and why, *Art Meas. Therm. Sci.* (2021) 313–335.
- [44] D. Cooke, S.G. Kandlikar, Effect of open microchannel geometry on pool boiling enhancement, *Int. J. Heat Mass Transf.* 55 (2012) 1004–1013, <https://doi.org/10.1016/j.ijheatmasstransfer.2011.10.010>.
- [45] A.M. Gheithaghy, H. Saffari, M. Mohebbi, Investigation pool boiling heat transfer in U-shaped mesochannel with electrodeposited porous coating, *Exp. Therm. Fluid Sci.* 76 (2016) 87–97, <https://doi.org/10.1016/j.expthermflusci.2016.03.011>.
- [46] S. Mori, K. Okuyama, Enhancement of the critical heat flux in saturated pool boiling using honeycomb porous media, *Int. J. Multiph. Flow.* 35 (2009) 946–951, <https://doi.org/10.1016/j.ijmultiphaseflow.2009.05.003>.
- [47] S.M. Kwark, G. Moreno, R. Kumar, H. Moon, S.M. You, Nanocoating characterization in pool boiling heat transfer of pure water, *Int. J. Heat Mass Transf.* 53 (2010) 4579–4587, <https://doi.org/10.1016/j.ijheatmasstransfer.2010.06.035>.
- [48] B. Shi, Y.-B. Wang, K. Chen, Pool boiling heat transfer enhancement with copper nanowire arrays, *Appl. Therm. Eng.* 75 (2015) 115–121, <https://doi.org/10.1016/j.applthermaleng.2014.09.040>.
- [49] A. Jaikumar, S.G. Kandlikar, Enhanced pool boiling heat transfer mechanisms for selectively sintered open microchannels, *Int. J. Heat Mass Transf.* 88 (2015) 652–661, <https://doi.org/10.1016/j.ijheatmasstransfer.2015.04.100>.
- [50] J.H. Lienhard IV, J.H. Lienhard V, A HEAT TRANSFER TEXTBOOK, fourth edition, Phlogist. Press. (2012) 766. 978-04864793161.
- [51] H. Lienhard, Peak pool boiling heat -flux measurements, *J. Heat Transfer.* (1973) 477–482.
- [52] S. Mt Aznam, S. Mori, A. Ogoshi, K. Okuyama, CHF enhancement of a large heated surface by a honeycomb porous plate and a gridded metal structure in a saturated pool boiling of nanofluid, *Int. J. Heat Mass Transf.* 115 (2017) 969–980, <https://doi.org/10.1016/j.ijheatmasstransfer.2017.07.089>.
- [53] J. Kim, S. Jun, J. Lee, J. Godinez, S.M. You, Effect of surface roughness on pool boiling heat transfer of water on a superhydrophilic aluminum surface, *J. Heat Transfer.* 139 (2017), 101501, <https://doi.org/10.1115/1.4036599>.
- [54] S.M. Kwark, M. Amaya, R. Kumar, G. Moreno, S.M. You, Effects of pressure, orientation, and heater size on pool boiling of water with nanocoated heaters, *Int. J. Heat Mass Transf.* 53 (2010) 5199–5208, <https://doi.org/10.1016/j.ijheatmasstransfer.2010.07.040>.
- [55] G. Chen, C.H. Li, Combined effects of liquid wicking and hydrodynamic instability on pool boiling critical heat flux by two-tier copper structures of nanowires and microgrooves, *Int. J. Heat Mass Transf.* 129 (2019) 1222–1231, <https://doi.org/10.1016/j.ijheatmasstransfer.2018.10.002>.
- [56] R.J. MacNamara, T.L. Lupton, R. Lupoi, A.J. Robinson, Enhanced nucleate pool boiling on copper-diamond textured surfaces, *Appl. Therm. Eng.* 162 (2019), <https://doi.org/10.1016/j.applthermaleng.2019.114145>.
- [57] Y. Yang, X. Ji, J. Xu, Pool boiling heat transfer on copper foam covers with water as working fluid, *Int. J. Therm. Sci.* 49 (2010) 1227–1237, <https://doi.org/10.1016/j.ijthermalsci.2010.01.013>.

- [58] Z.G. Xu, C.Y. Zhao, Experimental study on pool boiling heat transfer in gradient metal foams, *Int. J. Heat Mass Transf.* 85 (2015) 824–829, <https://doi.org/10.1016/j.ijheatmasstransfer.2015.02.017>.
- [59] M. Mahamudur Rahman, J. Pollack, M. Mccarthy, Increasing boiling heat transfer using low conductivity materials, *Sci. Rep.* 5 (2015) 12–14, <https://doi.org/10.1038/srep13145>.
- [60] M. Al Masri, S. Cioulachtjian, C. Veillas, I. Verrier, Y. Jourlin, J. Ibrahim, M. Martin, C. Pupier, F. Lefèvre, Nucleate boiling on ultra-smooth surfaces: explosive incipience and homogeneous density of nucleation sites, *Exp. Therm. Fluid Sci.* 88 (2017) 24–36, <https://doi.org/10.1016/j.exthermfluidsci.2017.05.008>.